https://dx.doi.org/10.1016/j.apcatb.2018.08.019

Tailoring the Rate-determining Step in Photocatalysis via Localized Excess Electrons for Efficient and Safe Air Cleaning

Jieyuan Li[a,b], Xing'an Dong[b], Yanjuan Sun[b], Guangming Jiang[b], Yinghao Chu[a], S. C. Lee[c], Fan Dong[*,b]

[a] College of Architecture and Environment, Sichuan University, Chengdu, Sichuan 610065, China

[b] Chongqing Key Laboratory of Catalysis and New Environmental Materials, College of Environment and Resources, Chongqing Technology and Business University, Chongqing 400067, China

[c] Department of Civil and Environmental Engineering, The Hong Kong Polytechnic University, Hong Kong, China

*Corresponding authors:

Fan Dong (dfctbu@126.com)

ABSTRACT

Regulating the rate-determining step in photocatalysis is crucial for advancing its application in environmental remediation. However, approaches for tailoring the rate-determining step have been largely overlooked. Herein, Ca-intercalated g-C_3N_4 is designed as a model photocatalyst to deeply understand the electron transportation behavior and the mechanisms of photocatalytic NO removal. The intercalation of Ca builds an interlayer channel for electron migration between g-C_3N_4 layers, which extends the sp^2 hybridized planes and enables the electrons to transform from a delocalized state to a localized state around Ca, leading to the formation of localized excess electrons (e^-_{ex}). Under visible light irradiation, these e^-_{ex} are subsequently captured by gas molecules for more efficient reactive oxygen species (ROS) generation and reactant activation. The ROS generated by Ca-intercalated g-C_3N_4 demonstrate stronger oxidation capability than those generated by pure CN. The ROS directly participate in photocatalytic NO oxidation and tailor the rate-determining step by decreasing the reaction activation energies, resulting in an overall increase in NO removal efficiency and a reduction in NO_2 production. The photocatalytic efficiency and selectivity have been significantly improved owing to the functionality of the e^-_{ex}. Using closely combined experimental and theoretical methods, this work provides a new approach for understanding the behaviors of e^-_{ex} in environmental photocatalysis and tailoring the rate-determining step to enhance reaction efficiency, achieving efficient and safe air purification.

Keywords: localized excess electrons; rate-determining step; photocatalysis; g-C_3N_4; DFT

1. Introduction

Semiconductor photocatalysis has been long recognized as a feasible and sustainable technology for environmental remediation, including NO_x purification,[1-4] volatile organic compound (VOC) removal[5, 6] and wastewater treatment.[7-9] Nevertheless, the photocatalytic activity and selectivity are still not satisfactory, especially when confronted with the accumulation of toxic intermediates.[10, 11] The inevitable generation of intermediates could cover the reactive sites of the photocatalysts and impede the overall reaction from reactants to final products. The conversion of intermediates to final products, which requires overcoming the high activation energy, appears to be the bottleneck in general environmental photocatalysis.[12-14] Thus, tailoring the rate-determining step to enhance reactant and intermediate conversion is of key importance in photocatalytic environmental remediation. To address this issue, in situ characterization technology and atomic level simulation, which could continuously survey the reaction process and provide insightful results, are conclusively required.

General modification strategies, including doping,[15-17] atomic vacancies[18, 19] and heterostructure construction,[20, 21] can transform the electrons from a delocalized state to a localized state, which can generate localized excess electrons (e^-_{ex}). However, the effects of e^-_{ex} on reactant activation and reactive oxygen species (ROS) generation have not been fully revealed. As illustrated in Scheme 1, the generation and delivery of e^-_{ex} are prerequisites for one semiconductor to participate in a photoredox reaction, thereby strongly impacting the optical absorption, charge transfer, and chemical reactivity.[22-24] Under light excitation, the e^-_{ex} prefer to be captured by reactants,[25, 26] which dominantly contribute to reinforced reactant activation and ROS generation.[27-29] Moreover, compared to the ROS with low activity (ROS-L; Scheme 1) that are induced by delocalized electrons, the e^-_{ex} can activate the O_2 molecules to generate

ROS with high oxidative capability (ROS-H).[30] The ROS-H directly initiate the photocatalytic reaction, which can reduce the reaction activation energies and increase the reaction rates of elementary reactions, hence overcoming the rate-determining step for more efficient pollutant conversion and target product generation.[31-33] Here, the e^-_{ex} could tailor the rate-determining step, which is a key limiting factor for increasing the overall photocatalysis efficiency.

Scheme 1

Considering the photocatalytic NO removal reaction as a case study, the accumulation of intermediate NO_2 is the bottleneck in improving overall reaction efficiency. The further oxidation of the toxic and stable intermediate NO_2 is the rate-determining step in NO removal.[34, 35] In this study, we designed the alkaline earth–intercalated g-C_3N_4 (henceforth denoted as CN) as model photocatalysts for tailoring charge transfer and electron localization because of their facile fabrication,[36, 37] visible-light response,[38, 39] and well-understood behavior regarding ion intercalation.[40-42] The Ca-intercalated CN (CN-Ca) was found to strongly assist e^-_{ex} generation, transfer, and capture in comparison with pure CN, significantly promoting spatial charge separation and ROS production.

Most importantly, the regulation of the rate-determining step in NO removal was first investigated via closely combined in situ diffuse reflectance infrared Fourier transform spectroscopy (DRIFTS) and density functional theory (DFT) simulations. The generation and delivery of e^-_{ex} in CN-Ca essentially contributes to O_2 activation, which subsequently provides ROS-H to overcome the rate-determining step, tuning the photocatalytic activity and selectivity for more efficient NO conversion and NO_2 inhibition. These results provide direct evidence that electron behavior definitively tailors the rate-determining step in photocatalytic environmental remediation. Specifically, the e^-_{ex} are generated by Ca intercalation and then captured by the gas

molecules to promote reactant activation and ROS generation under light irradiation. The reaction activation energy is reduced, thereby increasing reaction rate of the key elementary reaction and achieving more efficient and safe NO removal. Based on this success, various calculations, including the activation of CO, CO_2, NO_2, methanal, and toluene on Ca-CN, were performed to extend the knowledge base. The results agreed well with the case of NO. Consequently, we offer the general perspective that understanding the effect of e^-_{ex} on the rate-determining step is crucial for improving the performance of photocatalysts in many environmental and energy-related applications.

2. Experimental section

2.1 DFT calculations

All the spin-polarized DFT-D2 calculations were performed by the "Vienna ab initio simulation package (VASP 5.4.1)" using a generalized gradient correlation functional.[43] The cut-off energy was set to 450 eV within the framework of the projector-augmented wave method. The Gaussian smearing width was set to 0.2 eV. The Brillouin zone was sampled with a 5 × 5 × 1 K points. A hybrid Heyd–Scuseria–Ernzerhof (HSE06) method was utilized to predict the exact band structures.[44] The climbing image nudged elastic band (CI-NEB) method was applied to locate the minimum energy pathway from the initial state (IS) to its final state (FS).[45] The transition state (TS) was validated with a single imaginary frequency. The obtained electrons of specific atoms and molecules, Δq, were calculated with the Bader method,[46] where positive and negative values correspond to electron depletion and accumulation, respectively.

The adsorption energy, E_{ads}, is defined as

$$E_{ads} = E_{tot} - (E_{CN} + E_{mol}) , \quad (1)$$

where E_{tot}, E_{CN}, and E_{mol} refer to the total energy of the adsorption structures, g-C_3N_4 structures, and isolated molecules, respectively.

The formation energy, E_f, for Ca intercalation is defined as

$$E_f = E_{CN\text{-}Ca} - (E_{CN} + E_{metal}), \quad (2)$$

where $E_{CN\text{-}Ca}$, E_{CN}, and E_{metal} refer to the total energies of CN-Ca, pure CN, and induced Ca metal, respectively. The energy of a metal was calculated from its unit cell.

2.2 Photocatalysts fabrication

All chemicals used in this study were of analytical grade without additional treatment. The CN-Ca was fabricated via in situ co-pyrolysis. In a typical procedure, thiourea and $Ca(NO_3)_2$ were used as the precursors. Ten grams of thiourea and a known amount of $Ca(NO_3)_2$ (molar ratios of 3%, 5%, and 10%, relative to the experimentally obtained CN) were added to an alumina crucible with 30 mL of deionized water and then dried at 80 ℃ to induce re-crystallization. The covered crucible was then calcined at 550 ℃ in air for 2 h using a muffle furnace. After naturally cooling to room temperature, the as-prepared samples were collected. The CN-Ca with molar ratios of 1%, 3%, and 5% were labeled as CN-Ca1, CN-Ca3 and CN-Ca5, respectively. As will be discussed later, all the three CN-Ca samples manifested similar patterns in photocatalytic activities and characterizations. Thus CN-Ca3 was presented as a prototype, corresponding results of CN-Ca1 and CN-Ca5 were listed in the Supplementary Materials.

2.3 Characterization

The crystal phases of the samples were analyzed using X-ray diffraction (XRD) with CuKα radiation (Model D/max RA; Rigaku Co., Tokyo, JPN). The surface properties were investigated using X-ray photoelectron spectroscopy (XPS) with AlKα X-rays (Thermo ESCALAB 250; Thermo Scientific, Waltham, MA, USA). The morphologies were examined with scanning

126 electron microscopy (SEM; Model JSM-6490; JEOL, Tokyo, JPN) and transmission electron
127 microscopy (TEM; Model JEM-2010; JEOL, Tokyo, JPN). Ultraviolet-visible (UV-vis) diffuse
128 reflectance spectrometry was characterized using a scanning UV-vis spectra-photometer (UV-
129 2550; Shimadzu, Tokyo, JPN) equipped with an integrating sphere. Time-resolved fluorescence
130 emission spectra were measured using a fluorescence spectrophotometer (FLSP920; Edinburgh
131 Instruments, Livingston, GBR) at room temperature. The electron paramagnetic resonance (EPR)
132 characterization (FLSP920) of the as-prepared photocatalysts was carried out at 77 K. Electron
133 spin resonance (ESR) spectra of chemical radicals were obtained on a JES-FA200 spectrometer
134 (JEOL, Tokyo, JPN) to determine the involvement of the ROS in methanol dispersion and
135 aqueous dispersion for dimethyl pyridine N-oxide (DMPO)-$^{\bullet}O_2^-$ and DMPO-$^{\bullet}$OH, respectively.
136 2.4 Photocatalytic efficiency evaluation
137 The photocatalytic activities were investigated via the removal ratio of NO at ppb levels in an
138 in-house–designed continuous-flow reactor (Scheme S1 in the Supplementary Materials). A 150-
139 W commercial tungsten halogen lamp was placed vertically outside the reactor. A UV-cutoff
140 filter with a cutoff wavelength of 420 nm was utilized to remove UV light from the light beam.
141 For each test, 0.20 g of the prepared sample was dispersed in 50 mL of distilled water in a beaker.
142 The NO gas was obtained from a compressed gas cylinder, and the concentration of NO was
143 diluted to approximately 500 ppb in the air stream. The desired relative humidity level of the NO
144 flow was controlled at 50% by passing the NO-free air streams through a humidification
145 chamber. The gas streams were premixed completely using a gas blender. After adsorption–
146 desorption equilibrium was achieved, the lamp was activated. The concentration of NO was
147 continuously measured using a NO_x analyzer (Model 42c-TL; Thermo Scientific, Waltham, MA,
148 USA). The removal ratio, η, of NO was defined as

$$\eta = 1 - C/C_0 , \quad (3)$$

where C and C_0 are the concentrations of NO in the outlet and feeding stream, respectively.

2.5 In situ DRIFTS investigation

In situ DRIFTS measurements (Scheme S2 and Fig. S1) were applied in a TENSOR II FT-IR spectrometer (Bruker Corp., Billerica, MA, USA) equipped with an in situ diffuse-reflectance cell (Harrick Scientific Products Inc., Pleasantville, NY, USA) and a high-temperature reaction chamber (HVC). The reaction chamber was equipped with two coolant ports and three gas ports—through which, He, O_2, and 100 ppm of NO were fed into the reaction system. The total gas flow rate was 100 mL/min, and the concentration of NO was adjusted to 50 ppm by dilution with O_2. The chamber was enclosed within a dome with three windows: two for IR light entrance and detection and one for photocatalyst illumination. The observation window was made of UV quartz and the other two windows were made of ZnSe. A Xe lamp (MVL-210; Mejiro Genossen Inc., Tokyo, JPN) was used as the irradiation light source. Before measurements, prepared samples were pretreated at 300 °C for 20 min.

3 Results and discussion

3.1 Electrons localization design

The pure CN and CN-Ca were first constructed. As shown in the XRD patterns (Fig. 1a), two characteristic peaks, (001) and (002), at 13.1° and 27.4° respectively, reflect the generation of graphitic-like layered structures in CN.[38, 47] The (002) peak in CN-Ca is notably left-shifted in comparison with that of the pure CN (Fig. 1b), which can be attributed to the extension of the interlayer distance caused by the incorporation of Ca atoms between the layers. Thus, the intercalation of Ca between the layers of CN was realized. Moreover, the Ca is well defined in the XPS patterns (Fig. 1c and 1d). Typical SEM and TEM images (Fig. S2) indicate that Ca

inducement does not influence the morphology of CN, which consists of curved layers. The C, N, and Ca signals can be detected in the field emission SEM energy dispersive X-ray spectroscopy mappings (Fig. S3), verifying the homogeneous distribution of these elements. Additionally, the specific area, S_{BET}, (Table S1) and pore volume of CN-Ca are slightly reduced compared with CN, indicating that Ca intercalation blocks some surface accessibility. However, as will be discussed later, this reduction does not lead to any drop in photocatalytic activity, indicating that the S_{BET} and porous texture are not crucial parameters for determining the catalytic properties.

Fig. 1

The micro structures of CN-Ca at the atomic level were identified using the DFT calculations (Fig. S4). The Ca atoms tended to be located between the layers of CN, which agrees with the XRD patterns. The spatial distribution of electrons around Ca atoms was then calculated with the electronic localization function (ELF). The results indicate that Ca builds covalent interactions between the surface and subsurface of CN (Fig. 2a), which extends the π-conjugation system of CN to assemble delocalized electrons to form localized states around Ca atoms. The as-generated covalent bonding between Ca and C/N atoms can lead to the accumulation of e^-_{ex}, as depicted by the charge difference density (top view in Fig. 2b). These accumulated e^-_{ex} could further transfer between CN layers through the interlayer Ca channel (side view in Fig. 2c). This transfer route for e^-_{ex} is also proven by the calculated Bader effective charge, Δq, (Fig. S5), resulting in e^-_{ex} accumulation within this "triangle" region (Fig. 1f). This new electron localization pattern may strongly benefit light absorption and spatial charge separation. Most importantly, as the localized electrons can be accessed within this "triangle" region, more intense electron exchange is expected between the reactants and catalyst surface under light irradiation, leading to more

efficient reactant activation and ROS generation. Thus, the photocatalysis reaction process can be tailored via the e^-_{ex}–driven mechanism.

Fig. 2

3.2 Photocatalytic efficiency and photochemical properties evaluation

The photocatalytic efficiency was assessed towards NO removal under visible-light illumination (Fig. 3a and S6). The maximum NO removal ratios were reached in approximately 5 minutes for the CN and CN-Ca samples: 36.02% and 54.78%, respectively. The CN-Ca exhibited significantly enhanced conversion efficiency in comparison with the CN. Thus, the Ca intercalation is an effective approach for promoting the photocatalytic activity, which confirms our theoretical calculations. In addition, the catalytic stability of CN-Ca was investigated over five consecutive cycles (Fig. 3b). After the first run, it experienced slightly decreased activity, but the removal ratio remained constant for all remaining cycles (45%), which is nearly twice that of the pure CN (23%).

Fig. 3

The photo-electrochemical properties of the as-prepared samples were investigated to better understand the mechanism of photocatalytic efficiency enhancement. The calculated light absorption and UV-vis diffuse reflectance spectra (DRS; Fig 4a and S7) reveal that the red-shift band edge of the CN-Ca samples is present, unlike the pure CN; therefore, Ca intercalation extends the light absorption range in the visible-light region. The density of states (DOS; Fig. 4b) was calculated to survey the band structures. The band energy of pure CN was estimated to be 2.66 eV; consequently, the narrower band gap of CN-Ca (2.05 eV) guarantees higher light absorption. Moreover, the valence band (VB) and conduction band (CB) edges of CN-Ca are downshifted relative to those in CN. Thus, the band structure is tailored by Ca intercalation,

resulting in the enhanced photo-oxidation ability of the holes in CN-Ca. The elevated light absorption ability is essentially contributed by the electron localization, which provides broad light response and facilitations electrons hopping between the VB and CB.

The time-dependent fluorescence decay spectra were obtained to investigate the charge motion dynamics (Fig. 4c). In contrast to the pure CN, the lifetimes of carriers in CN-Ca were prolonged, confirming that the electron localization effectively boosts charge separation and transfer. The photoluminescence (PL) spectra (Fig. S8) further demonstrate that electron–hole recombination is indubitably inhibited. The solid state EPR (Fig. 4d) was investigated to evaluate the electron mobility of the as-prepared samples. It indicates that the π-conjugated delocalization in CN is significantly extended by Ca intercalation,[48] which implies that the e^-_{ex} in CN-Ca can move out of the delocalized sp^2 plane, subsequently accumulating around Ca atoms for more intense charge transfer with the reactants, contributing to reactant activation and ROS generation. The separated carriers can participate in photocatalytic reactions before their recombination. These photo-electrochemical properties demonstrate that the generation and delivery of e^-_{ex} in CN-Ca could promote the fast transfer and effective suppression of photo-excited charge carriers, consequently leading to enhanced photocatalytic efficiency and selectivity.

Fig. 4

Beyond the oxidation ability of light-generated holes, the photocatalytic activity is initiated through generated active radicals, such as ROS, for more efficient photo-oxidation reactions. The major ROS are detected by applying the DMPO spin-trapping ESR spectra in an ethanol dispersion for $^{\bullet}O_2^-$ (Fig. 5a) and aqueous dispersion for $^{\bullet}OH$ (Fig. 5b). It is worth noting that the amount of ROS, which provides more reactive radicals for NO conversion, is remarkably higher in CN-Ca than in pure CN. Based on the band structures of CN (Fig. S9), the generation of ROS

239 on CN originates from O_2 activation, along the route of $O_2 \rightarrow {}^{\bullet}O_2^- \rightarrow H_2O_2 \rightarrow {}^{\bullet}OH$,[28, 49-51]
240 hence, these experiments demonstrate that the effective capture of e^-_{ex} for O_2 activation is the
241 prerequisite for promoting photocatalytic NO oxidation.

242 **Fig. 5**

243 3.3 In situ DRIFTS investigation

244 To understand the reaction process and clarify the promotion mechanism in detail, in situ
245 DRIFTS were performed to measure the dynamic reaction intermediates and final products (Fig.
246 3; Fig. S10 shows the full-region spectra over all wavenumbers). The background spectrum was
247 recorded before NO injection. The NO absorption bands were detected once the injected NO
248 contacted the surfaces of CN (2195 cm^{-1}; Fig. 6a) and CN-Ca (2194 cm^{-1}; Fig. 6b) in the dark.[52,
249 53] Over time, the corresponding DRIFTS adsorption peak intensities increased, indicating the
250 gradual accumulation of NO on the photocatalysts. Meanwhile, the absorption bands of the
251 intermediate NO_2 (2070 cm^{-1}) were also observed. The species evolution (Fig. 6c) confirms that
252 more NO and NO_2 were accumulated on the CN-Ca than on the pure CN, which demonstrates
253 that the e^-_{ex} efficiently contribute to the activation of reactants and intermediate products. Owing
254 to the regulation of the sp^2 system of CN-Ca, the e^-_{ex} tended to transfer out of the π-conjugated
255 surface for more intense electron donation to NO_x compounds and O_2 molecules for activation.
256 Hence, NO oxidation at atmospheric temperature took place as NO_2^- (1090 cm^{-1} in CN and 1095
257 cm^{-1} in CN-Ca) and NO_3^- (1009 cm^{-1} in CN and 1014 cm^{-1} in CN-Ca) were detected.[54, 55]
258 Many more products accumulated on CN-Ca than on CN, which confirms that the extension of
259 π-conjugation could increase the catalytic process.[56, 57]

260 **Fig. 6**

After the adsorption equilibrium (Ads. equil.) was reached, the DRIFTS of CN (Fig. 6d) and CN-Ca (Fig. 6e) were continuously monitored under visible-light irradiation. In comparison with the "Ads. equil." spectrum, the adsorption intensities of the intermediates and final products observably increased, which illustrates that the photocatalysts are sensitive to visible-light and able to effectively catalyze the NO oxidation. Most importantly, comparing the intermediate NO_2 and final product evolution on CN and CN-Ca (Fig. 6f) indicates that CN-Ca can better inhibit the accumulation of intermediate NO_2, which catalyzes the NO oxidation more effectively to overcome the rate-determining step, leading to more accumulation of the target products (i.e., NO_2^- and NO_3^-). It can therefore be concluded that the photocatalytic activity and selectivity for the final products are significantly reinforced by Ca intercalation–induced e^-_{ex} utilization, which promotes the adsorption and activation of reactants, suppresses the accumulation of intermediate products, and enhances the selectivity for the target products. All the observed DRIFTS bands of the adsorbed species are listed in Tables S2–S5. The proposed primary reaction mechanism for NO photocatalytic oxidation by ROS is

$$\text{CN/CN-Ca} + h\nu \rightarrow e^- + h^+ \quad (4)$$

$$e^- + O_2 \rightarrow {}^{\bullet}O_2^- \quad (5)$$

$${}^{\bullet}O_2^- + 2H^+ + e^- \rightarrow H_2O_2 \quad (6)$$

$$H_2O_2 + e^- \rightarrow {}^{\bullet}OH + OH^- \quad (7)$$

$$NO + {}^{\bullet}O_2^- \rightarrow NO_2 \quad (8)$$

$$NO_2 + {}^{\bullet}O_2^- \rightarrow NO_3^- \quad (9)$$

$$NO + {}^{\bullet}OH \rightarrow HNO_2 \quad (10)$$

$$NO_2 + {}^{\bullet}OH \rightarrow HNO_3 \quad (11)$$

3.4 Reaction coordinates calculations

As the e^-_{ex} facilitate charge transfer between the photocatalysts' surface and O_2 molecules, which definitively contributes to ROS generation and photocatalytic efficiency enhancement, the electron behavior at the atomic level needs to be further investigated. The adsorption and activation of one O_2 molecule on CN (Fig. 7a) and CN-Ca (Fig. 7c) were calculated via DFT. More intense charge transfer was observed between O_2 and CN-Ca than between O_2 and CN. The adsorption energy, E_{ads}, for the O_2 molecule increased from -0.19 eV (CN) to -0.54 eV (CN-Ca), resulting in the O_2 accepting more e^-_{ex} from CN-Ca (-0.46 e) than from pure CN (-0.23 e). Under light irradiation, the O_2 on CN-Ca were more easily activated to form ROS-H, which possess higher oxidizability than the ROS-L in CN. The ROS-H directly participate in the photo-oxidation reaction of NO, overcoming the rate-determining step of elementary reactions, which enhances the photo-oxidizability of CN-Ca compared with CN (Scheme 1).

Fig. 7

Additionally, we calculated the activation of multiple O_2 molecules (Fig. 7b, 7d and S11). The average Bader effective charges, Δq (avg.), and adsorption energies, E_{ads} (avg.), were increased in CN-Ca in comparison with those in CN. These results clearly indicate that the e^-_{ex} in CN-Ca significantly facilitate ROS generation, leading to the production of more $^{\bullet}O_2^-$ and $^{\bullet}OH$, which well match with the ESR results (Fig. 5). The more-accumulated ROS on CN-Ca can oxidize NO for more efficient conversion than that afforded by CN. The electron localization–induced ROS generation is predicted to contribute to the enhancement of photocatalytic activity and selectivity.

In order to elucidate the primary reaction mechanism proposed from the in situ DRIFTS measurements, the ROS-driven reaction pathways were calculated using the CI-NEB method with a single imaginary frequency (*f/i*; Table S6) verified for NO photo-oxidation by $^{\bullet}O_2^-$ (Fig. 7e) and $^{\bullet}OH$ (Fig. 7f). Based on the detection of the most stable products at each step by the in-

situ DRIFTS and ESR spectra, NO oxidation by $^{\bullet}O_2^-$ is composed of three elementary reactions (path 1–3). As can be seen in Fig. 7e, O_2 activation is more energy-favorable on CN-Ca than on CN owing to an increase of energy release (-0.45 eV, path 1). Subsequently, NO was smoothly oxidized to NO_2 on CN-Ca without an energy barrier, resulting in a spontaneous oxidation process (path 2). In contrast, the same reaction requires 0.44 eV of activation energy, ΔE_a, to proceed on CN. Furthermore, the reaction energies, ΔE_r, (Fig. S12 and S13) of path 2 illustrate that the e^-_{ex}-induced ROS generation alters the reaction from energy absorption on CN (0.13 eV) to energy release on CN-Ca (-2.06 eV). Then, the NO_2 oxidation was calculated (path 3), its ΔE_r exhibits patterns similar to those of path 2. However, the ΔE_a—CN (0.63 eV) and CN-Ca (0.33 eV)—are higher than those of path 2, confirming that NO_2 is more stable, being more difficult to oxidize, which causes NO_2 oxidation to be the rate-determining step in NO photo-oxidation.

Calculations for NO oxidation by $^{\bullet}OH$ were further conducted (Fig. 7f)—the results agree with those for $^{\bullet}O_2^-$. Specifically, in the rate-determining step of NO_2 oxidation (path 5), NO_2 is more preferably oxidized by $^{\bullet}OH$ on CN-Ca than on pure CN, with a significant decrease of ΔE_a from 0.54 eV to 0.17 eV. Based on these results, the primary rate-determining step was concluded to be NO_2 oxidation via path 3. The second-largest energy barrier was observed in path 5. In general, increasing the activation of a reactant on a catalyst reduces the energy barrier for a chemical reaction. The e^-_{ex} in CN-Ca were deduced to effectively promote reactant activation, hence generating more ROS-H to catalyze NO oxidation with lower ΔE_a and higher reaction rates. These theoretical calculations directly expose the primary reaction processes of NO photo-oxidation on CN, demonstrating that the enhanced photocatalytic efficiency and selectivity are dominantly caused by the effective utilization of e^-_{ex}.

3.5 Pollutants activation calculations

Based on the current knowledge base, we further conducted more theoretical calculations for a general perspective. As shown in Fig. 8, various gas molecules/pollutants, including NO, NO_2, CO, CO_2, methanal (CH_2O), and toluene (C_7H_8), can be more effectively activated by the e^-_{ex} in CN-Ca than by the delocalized electrons in CN. The number of transferred electrons and the adsorption energies of these molecules substantially enhanced for CN-Ca compared with CN (Table S7); these improvements were caused by the Ca intercalation–induced e^-_{ex} utilization.

Fig. 8

4. Conclusions

In summary, we have proposed and certified that the rate-determining step in NO photocatalytic removal can be rationally tailored via the localized excess electrons (e^-_{ex}). Using Ca intercalated g-C_3N_4 as a model photocatalyst to generate and assemble the e^-_{ex}, this work provided direct evidence that the light absorption and charge separation properties of g-C_3N_4 is significantly facilitated owing to the generation and transfer of the e^-_{ex}. Beyond that, more reactive oxygen species (ROS) with stronger oxidation capability were generated, which can directly initiate the photocatalysis reaction and regulated the rate-determining step to enhance the over-all photocatalytic efficiency, meanwhile reducing the toxic intermediate accumulation. Applying closely-combined experimental and theoretical methods, the rate-determining step in photocatalysis is firstly tailored via the e^-_{ex}-driven mechanism. This work reveals that understanding the effect of e^-_{ex} on the rate-determining step is crucial for improving the performance of photocatalysts in environmental and energy-related applications.

Acknowledgements

This work was supported by the National Key R&D project (Grant No. 2016YFC0204702), the National Natural Science Foundation of China (Grant Nos. 51478070, 21501016, and 21777011), the Innovative Research Team of Chongqing (Grant No. CXTDG201602014), the Natural Science Foundation of Chongqing (Grant No. cstc2017jcyjBX0052), the Plan for "National Youth Talents" of the Organization Department of the Central Committee, and the Youth Project in Science and Technology Innovation Program of Sichuan Province (Grant No. 17-YCG053). The authors also acknowledge the AM-HPC in Suzhou, China for computational support.

Appendix A. Supplementary data

Supplementary Materials. The Supplementary Materials contains schematic illustrations for the continuous photocatalytic and in situ DRIFTS reactors, SEM and TEM images, elemental mappings, S_{BET} and pore volumes results, micro structures, Bader effective charges around Ca atoms, photocatalytic efficiencies, UV-Vis DRS and PL spectra of CN-Ca at different Ca concentrations, band structures, full-region in situ DRIFTS spectra, assignments of all the observed DRIFTS bands, O_2 adsorption calculations, calculated imaginary frequencies, detailed minimum energy pathways for NO oxidation, and a summary of reactant activation calculations.

REFERENCES

[1] G. H. Dong, L. P. Yang, F. Wang, L. Zang, C. Y. Wang, ACS Catal. 6 (2017) 6511-6519.
[2] C. C. Yu, V. H. Nguyen, J. Lasek, J. C. S. Wu, Appl. Catal. B: Environ. 219 (2017) 391-400.
[3] W. Cui, J. Y. Li, F. Dong, Y. Sun, G. Jiang, W. Cen, S. C. Lee, Z. Wu, Environ. Sci. Technol. 38 (2017) 10746-10753.
[4] J. Y. Li, X. A. Dong, Y. J. Sun, W. L. Cen, F. Dong, Appl. Catal. B: Environ. 226 (2018) 269-277.
[5] Y. M. Ji, J. Zhao, H. Terazono, K. Misawa, N. P. Levitt, Y. X. Li, Y. Lin, J. F. Peng, Y. Wang, L. Duan, B. W. Pan, F. Zhang, X. D. Feng, T. C. An, W. Marrero-Ortiz, J. Secrest, A. L.

371 Zhang, K. Shibuya, M. J. Molina, R. Y. Zhang, Proc. Natl. Acad. Sci. U. S. A. (2017)
372 201705463.
373 [6] A. H. Mamaghani, F. Haghighat, C. S. Lee, Appl. Catal. B: Environ. 203 (2017) 247-269.
374 [7] H. Li, F. Qin, Z. Yang, X. Cui, J. Wang, L. Z. Zhang, J. Am. Chem. Soc. 139 (2017) 3513.
375 [8] G. S. Liu, S. J. You, Y. Tang, N. Q. Ren, Environ. Sci. Technol. 51 (2017) 2339-2346.
376 [9] J. Romao, G. Mul, ACS Catal. 6 (2016) 1254-1262.
377 [10] J. Kou, C. Lu, J. Wang, Y. Chen, Z. Xu, R. S. Varma, Chem. Rev. 117 (2017) 1445.
378 [11] Q. Guo, C. Zhou, Z. Ma, Z. Ren, H. Fan, X. Yang, Chem. Soc. Rev. 45 (2016) 3701.
379 [12]D. G. Gong, V. P. Subramaniam, J. G. Highfield, Y. X. Tang, Y. K. Lai, Z. Chen, ACS
380 Catal. 1 (2011) 864-871.
381 [13] E. S. Kai, T. F. Berto, W. Eisenreich, A. Jentys, O. Y. Gutiérrez, J. A. Lercher, ACS Catal.
382 7 (2017) 3236-3244.
383 [14] B. Limburg, E. Bouwman, S. Bonnet, ACS Catal. 6 (2016) 5273-5284.
384 [15] G. Gao, Y. Jiao, E. R. Waclawik, A. Du, J. Am. Chem. Soc. 138 (2016) 6292.
385 [16] S. Guo, Z. Deng, M. Li, B. Jiang, C. Tian, Q. Pan, H. Fu, Angew. Chem. Int. Ed. 55 (2016)
386 1830.
387 [17] J. Li, L. Cai, J. Shang, Y. Yu, L. Z. Zhang, Adv. Mater. 28 (2016) 4059-4064.
388 [18] Z. Zhou, J. Liu, R. Long, L. Li, L. Guo, O. V. Prezhdo, J. Am. Chem. Soc. 139 (2017)
389 6707-6717.
390 [19] G. Dong, D. L. Jacobs, L. Zang, C. Wang, Appl. Catal. B: Environ. 218 (2017) 515-524.
391 [20] M. Zhu, S. Kim, L. Mao, M. Fujitsuka, J. Zhang, X. Wang, T. Majima, J. Am. Chem. Soc.
392 139 (2017) 13234-13242.
393 [21] H. Wang, L. Zhang, Z. Chen, J. Hu, S. Li, Z. Wang, J. Liu, X. Wang, Chem. Soc. Rev. 43
394 (2014) 5234-5244.
395 [22] K. Lee, Q. Kim, S. An, J. An, J. Kim, B. Kim, W. Jhe, Proc. Natl. Acad. Sci. U. S. A. 111
396 (2014) 5784-5789.
397 [23] Z. Lin, L. Li, L. Yu, W. Li, G. Yang, J. Mater. Chem. A 5 (2017) 5235-5259.
398 [24] M. Setvin, C. Franchini, X. Hao, M. Schmid, A. Janotti, M. Kaltak, V. D. W. Cg, G. Kresse,
399 U. Diebold, Phys. Rev. Lett. 113 (2014) 163-248.
400 [25] N. Q. Le, I. V. Schweigert, J. Phys. Chem. C 121 (2017) 14254-14260.
401 [26] M. Setvin, X. Hao, B. Daniel, J. Pavelec, Z. Novotny, G. S. Parkinson, M. Schmid, G.
402 Kresse, C. Franchini, U. Diebold, Angew. Chem. Int. Ed. 53 (2014) 4714-1716.
403 [27] Y. F. Li, U. Aschauer, J. Chen, A. Selloni, Acc. Chem. Res. 47 (2014) 3361-3368.
404 [28] Y. Nosaka, A. Y. Nosaka, Chem. Rev. 117 (2017) 11302-11336.
405 [29] T. Hirakawa, H. Kominami, A. B. Ohtani, Y. Nosaka, J. Phys. Chem. B 105 (2001) 6993-
406 6999.
407 [30] T. L. Thompson, J. T. Yates, Chem. Rev. 10 (2006) 4428-4453.
408 [31] M. R. Hoffmann, S. T. Martin, W. Y. Choi, D. W. Bahnemann, Chem. Rev. 95 (1995) 69-
409 96.
410 [32] B. Tryba, M. Toyoda, A. W. Morawski, R. Nonaka, M. Inagaki, Appl. Catal. B:Environ. 71
411 (2007) 163-168.
412 [33] J. B. Sambur, P. Chen, J. Phys. Chem. C 120 (2016) 20668-20676.
413 [34] F. Dong, Z. Zhao, Y. Sun, Y. Zhang, S. Yan, Z. Wu, Environ. Sci. Technol. 49 (2015)
414 12432-12440.
415 [35] Z. H. Ai, W. K. Ho, S. C. Lee, L. Z. Zhang, Environ. Sci. Technol. 43 (2009) 4143-4150.
416 [36] F. Dong, L. Wu, Y. Sun, M. Fu, Z. Wu, S. C. Lee, J. Mater. Chem. 21 (2011) 15171-15174.

[37] Y. S. Jun, E. Z. Lee, X. C. Wang, W. H. Hong, G. D. Stucky, A. Thomas, Adv. Funct. Mater. 23 (2013) 3661–3667.
[38] X. C. Wang, K. Maeda, A. Thomas, K. Takanabe, G. Xin, J. M. Carlsson, K. Domen, M. Antonietti, Nat. Mater. 8 (2009) 76.
[39] Y. Li, S. Ouyang, H. Xu, X. Wang, Y. Bi, Y. Zhang, J. H. Ye, J. Am. Chem. Soc. 138 (2016) 13289-13297.
[40] J. Y. Li, W. Cui, Y. Sun, Y. Chu, W. Cen, F. Dong, J. Mater. Chem. A 5 (2017) 9358.
[41] T. Xiong, W. Cen, Y. Zhang, F. Dong, ACS Catal. 6 (2016) 2462-2472.
[42] L. Chen, G. S. Shi, J. Shen, B. Q. Peng, B. W. Zhang, Y. Z. Wang, F. G. Bian, J. J. Wang, D. Y. Li, Z. Qian, G. Xu, G. P. Liu, J. R. Zeng, L. J. Zhang, Y. Z. Yang, G. Q. Zhou, M. H. Wu, H. P. Fang, Nature 550 (2017) 380-383.
[43] G. Kresse, J. Furthmuller, Comput. Mater. Sci. 6 (1996) 15-50.
[44] J. Heyd, J. Chem. Phys. 118 (2003) 8207-8215.
[45] G. Henkelman, B. P. Uberuaga, H. Jónsson, J. Chem. Phys. 113 (2000) 9901-9904.
[46] R. Bader, Atoms in Molecules: A Quantum Theory. Oxford University Press 1994.
[47] L. H. Lin, H. H. Ou, Y. F. Zhang, X. C. Wang, ACS Catal. 6 (2016) 3921-3931.
[48] G. Zhang, M. Zhang, X. Ye, X. Qiu, S. Lin, X. C. Wang, Adv. Mater. 26 (2014) 805.
[49]T. Hirakawa, Y. Nosaka, J. Phys. Chem. C 112 (2008) 15818-15823.
[50]F. Dong, Z. Wang, Y. Li, W. K. Ho, S. C. Lee, Environ. Sci. Technol. 48 (2014) 10345-10353.
[51] A. Kudo, Y. Miseki, Chem. Soc. Rev. 38 (2009) 253-278.
[52] K. Hadjiivanov, V. Avreyska, A. D. Klissurski, T. Marinova, Langmuir 18 (2012) 1619-1625.
[53] T. Weingand, S. Kuba, K. Hadjiivanov, H. Knözinger, J. Catal. 209 (2002) 539-546.
[54] L. Jaan, J. R. Ohlsen, Prog. in Inorg. Chem. 27 (2007) 465-513.
[55] L. Zhong, Y. Yu, W. Cai, X. Geng, Q. Zhong, Phys. Chem. Chem. Phys. 17 (2015) 15036.
[56] J. Y. Li, S. Yin, F. Dong, W. Cen, Y. Chu, ACS Appl. Mater. Interfaces 9 (2017) 19861-19869.
[57] D. Guo, R. Shibuya, C. Akiba, S. Saji, T. Kondo, J. Nakamura, Science 351 (2016) 361.

Figure Captions

Scheme 1. Design diagram for localized excess electrons that decrease the reaction activation energies and increase the photocatalysis efficiency.

Fig. 1 XRD patterns for CN and CN-Ca (a), enlarged profiles of the (002) diffraction region in XRD patterns (b), XPS survey (c) and Ca scanning (b) spectra.

Fig. 2 ELF for CN-Ca (a), top view (b) and side view (c) of the charge difference density distribution for CN-Ca. [Charge accumulation and depletion are in blue and yellow, respectively; the isosurfaces are both set to 0.0075 eV $Å^{-3}$; blue, green, and red spheres represent N, C, and Ca atoms, respectively].

Fig. 3 Photocatalytic activity evaluation of CN and CN-Ca towards NO purification under visible light irradiation (a) and cycling test for CN-Ca (b).

Fig. 4 Calculated light absorption spectra and experimental UV-vis DRS spectra (a), calculated DOS (b), where the Fermi levels are both set to 0 eV, (c) ns-level time-resolved fluorescence spectra and (d) EPR spectra.

Fig. 5 DMPO ESR spectra in methanol dispersion for $^{\bullet}O_2^-$ (a) and in aqueous dispersion of $^{\bullet}OH$ (b).

Fig. 6 Survey of reaction processes on CN and CN-Ca: (a–c) in situ DRIFTS spectra in selected region of wavenumbers and species evolution of NO adsorption in the dark and (d–f) oxidation under visible light irradiation.

Fig. 7 Calculated results for ROS generation and reaction pathways: Charge difference density distribution of (a) O_2@CN, (b) $4O_2$@CN, (c) O_2@CN-Ca, and (d) $4O_2$@CN-Ca; calculated CI-NEB reaction pathways for NO photo-oxidation by (e)

$^{\bullet}O_2^-$ and (f) $^{\bullet}OH$. [Charge accumulation and depletion are in blue and yellow, respectively; the isosurfaces are all set to 0.005 eV $Å^{-3}$; blue, green, red, and gold spheres represent N, C, Ca, and O atoms respectively; negative values for E_{ads} indicate heat release.]

Fig. 8 Reactant activation comparison: calculated charge density difference of (a, g) NO, (b, h) NO_2, (c, i) CO, (d, j) CO_2, (e, k) methanal (CH_2O), and (f, l) toluene (C_7H_8) adsorption on (a–f) CN and (g–l) CN-Ca. [Blue, green, red, gold, and pink spheres represent N, C, Ca, O, and H atoms, respectively; all lengths are given in Å.]

Scheme 1

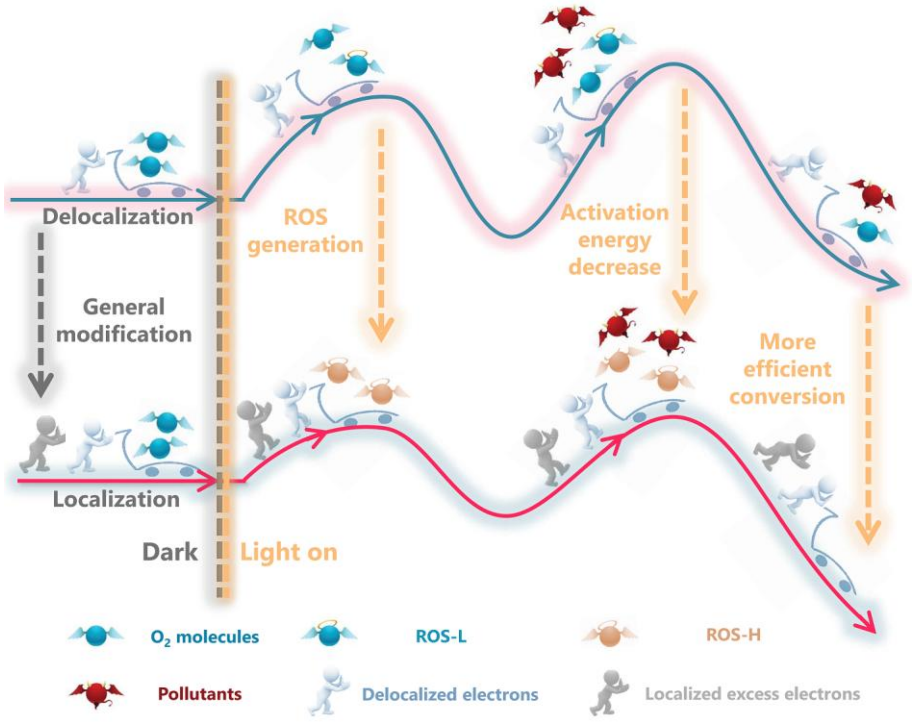
Delocalization
General modification
Localization
Dark
Light on
ROS generation
Activation energy decrease
More efficient conversion
O_2 molecules
ROS-L
ROS-H
Pollutants
Delocalized electrons
Localized excess electrons

Fig. 1

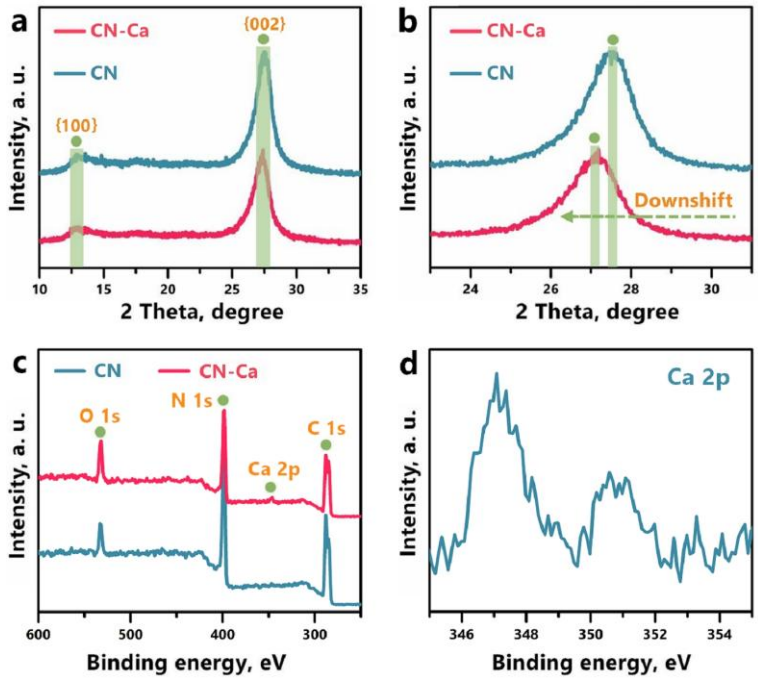
a
CN-Ca
CN
{002}
{100}
Intensity, a. u.
2 Theta, degree
b
CN-Ca
CN
Downshift
Intensity, a. u.
2 Theta, degree
c
CN
CN-Ca
O 1s
N 1s
C 1s
Ca 2p
Intensity, a. u.
Binding energy, eV
d
Ca 2p
Intensity, a. u.
Binding energy, eV

Fig. 2

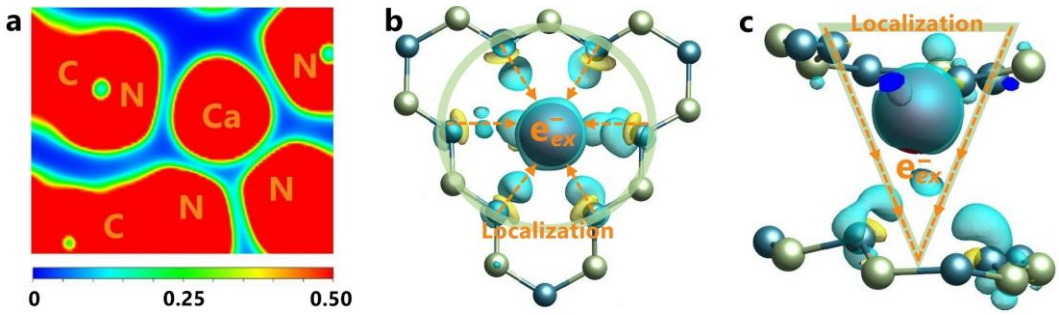
a
C
N
Ca
N
N
C
0
0.25
0.50
b
e⁻ex
Localization
c
Localization
e⁻ex

Fig. 3

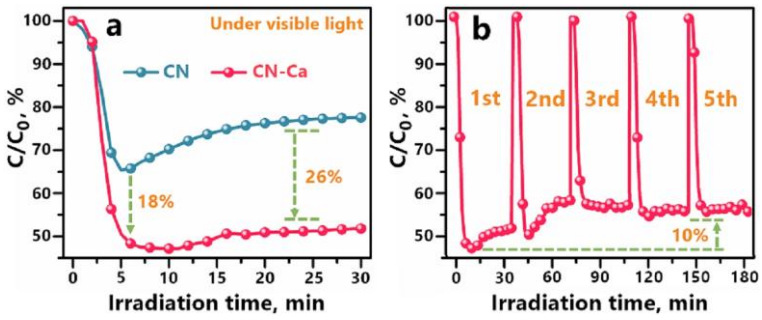
a
Under visible light
CN
CN-Ca
18%
26%
C/C0, %
Irradiation time, min
b
1st
2nd
3rd
4th
5th
10%
C/C0, %
Irradiation time, min

Fig. 4

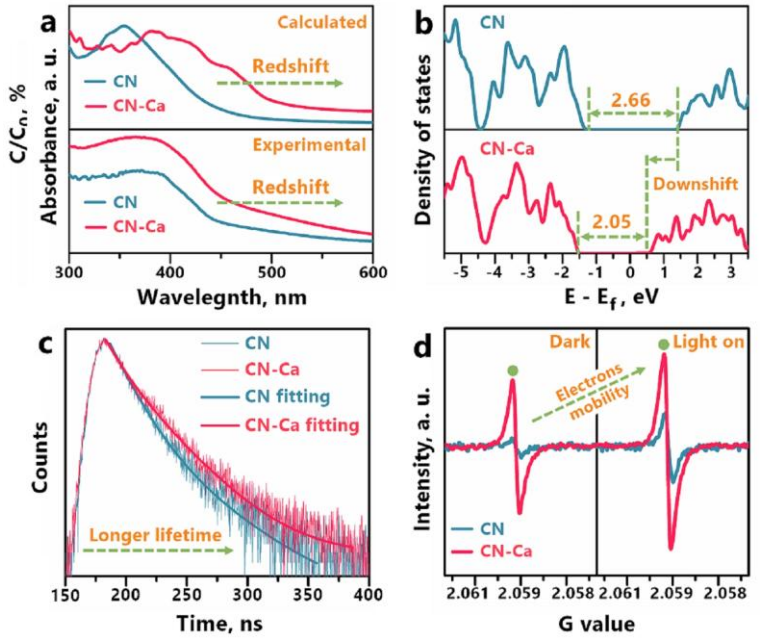
a
Calculated
Redshift
CN
CN-Ca
Experimental
Redshift
CN
CN-Ca
C/Cn, %
Absorbance, a. u.
Wavelegnth, nm
b
CN
2.66
CN-Ca
Downshift
2.05
Density of states
E - Ef, eV
c
CN
CN-Ca
CN fitting
CN-Ca fitting
Longer lifetime
Counts
Time, ns
d
Dark
Light on
Electrons mobility
CN
CN-Ca
Intensity, a. u.
G value

Fig. 5

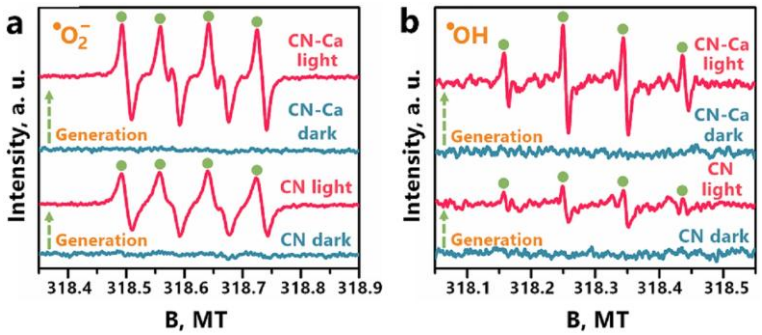
a
$^{\bullet}O_2^-$
CN-Ca light
CN-Ca dark
CN light
CN dark
Generation
Intensity, a. u.
318.4 318.5 318.6 318.7 318.8 318.9
B, MT
b
$^{\bullet}OH$
CN-Ca light
CN-Ca dark
CN light
CN dark
Generation
Intensity, a. u.
318.1 318.2 318.3 318.4 318.5
B, MT

Fig. 6

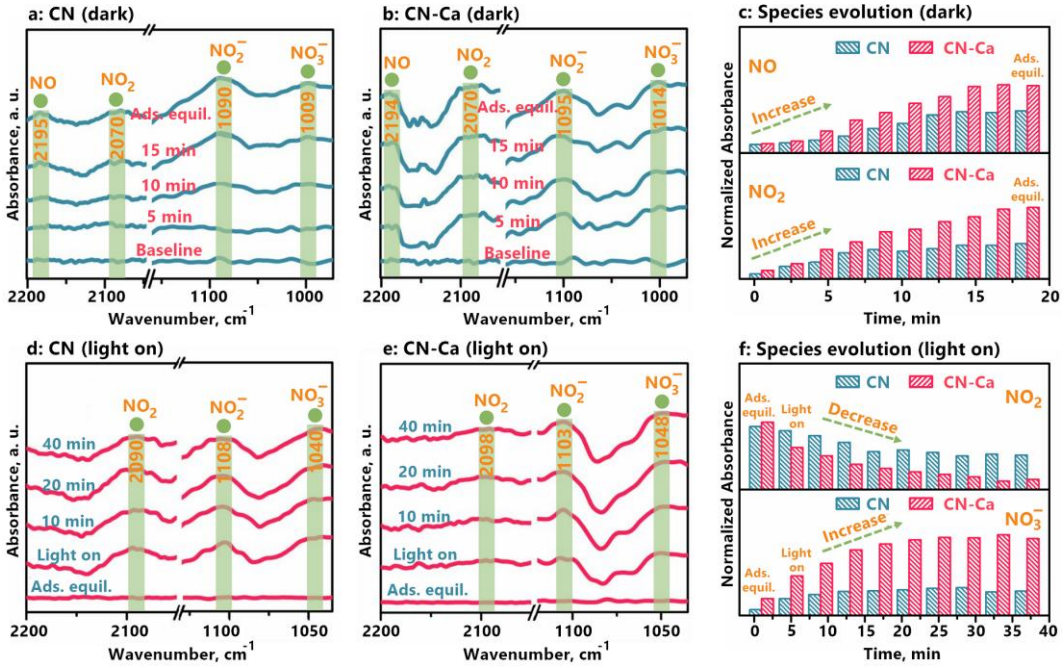
a: CN (dark)
NO
NO_2
NO_2^-
NO_3^-
2195
2070
1090
1009
Ads. equil.
15 min
10 min
5 min
Baseline
Absorbance, a. u.
2200 2100 1100 1000
Wavenumber, cm^{-1}
b: CN-Ca (dark)
2194
2070
1095
1014
Ads. equil.
15 min
10 min
5 min
Baseline
Absorbance, a. u.
2200 2100 1100 1000
Wavenumber, cm^{-1}
c: Species evolution (dark)
CN
CN-Ca
NO
Ads. equil.
Increase
NO_2
Normalized Absorbance
0 5 10 15 20
Time, min
d: CN (light on)
NO_2
NO_2^-
NO_3^-
40 min
20 min
10 min
Light on
Ads. equil.
2090
1108
1040
Absorbance, a. u.
2200 2100 1100 1050
Wavenumber, cm^{-1}
e: CN-Ca (light on)
2098
1103
1048
Absorbance, a. u.
2200 2100 1100 1050
Wavenumber, cm^{-1}
f: Species evolution (light on)
CN
CN-Ca
Ads. equil.
Light on
Decrease
NO_2
Increase
NO_3^-
Normalized Absorbance
0 5 10 15 20 25 30 35 40
Time, min

Fig. 7

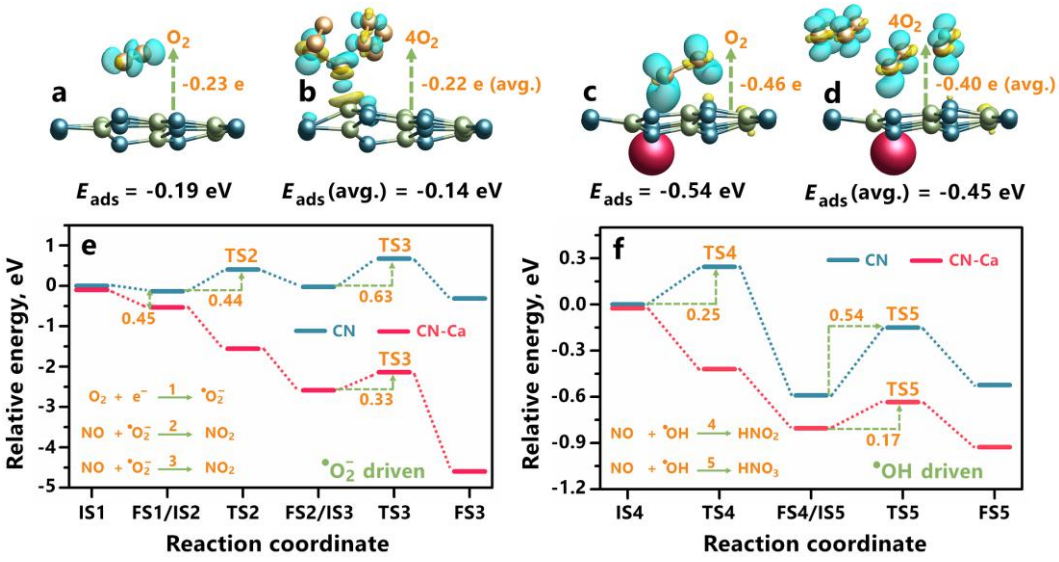
a
O_2
-0.23 e
b
$4O_2$
-0.22 e (avg.)
c
O_2
-0.46 e
d
$4O_2$
-0.40 e (avg.)
E_{ads} = -0.19 eV
E_{ads}(avg.) = -0.14 eV
E_{ads} = -0.54 eV
E_{ads}(avg.) = -0.45 eV
e
Relative energy, eV
TS2
TS3
0.44
0.63
0.45
CN
CN-Ca
TS3
0.33
$O_2 + e^- \xrightarrow{1} {}^{\bullet}O_2^-$
$NO + {}^{\bullet}O_2^- \xrightarrow{2} NO_2$
$NO + {}^{\bullet}O_2^- \xrightarrow{3} NO_2$
${}^{\bullet}O_2^-$ driven
IS1
FS1/IS2
TS2
FS2/IS3
TS3
FS3
Reaction coordinate
f
Relative energy, eV
TS4
CN
CN-Ca
0.25
0.54
TS5
TS5
0.17
$NO + {}^{\bullet}OH \xrightarrow{4} HNO_2$
$NO + {}^{\bullet}OH \xrightarrow{5} HNO_3$
${}^{\bullet}OH$ driven
IS4
TS4
FS4/IS5
TS5
FS5
Reaction coordinate

Fig. 8

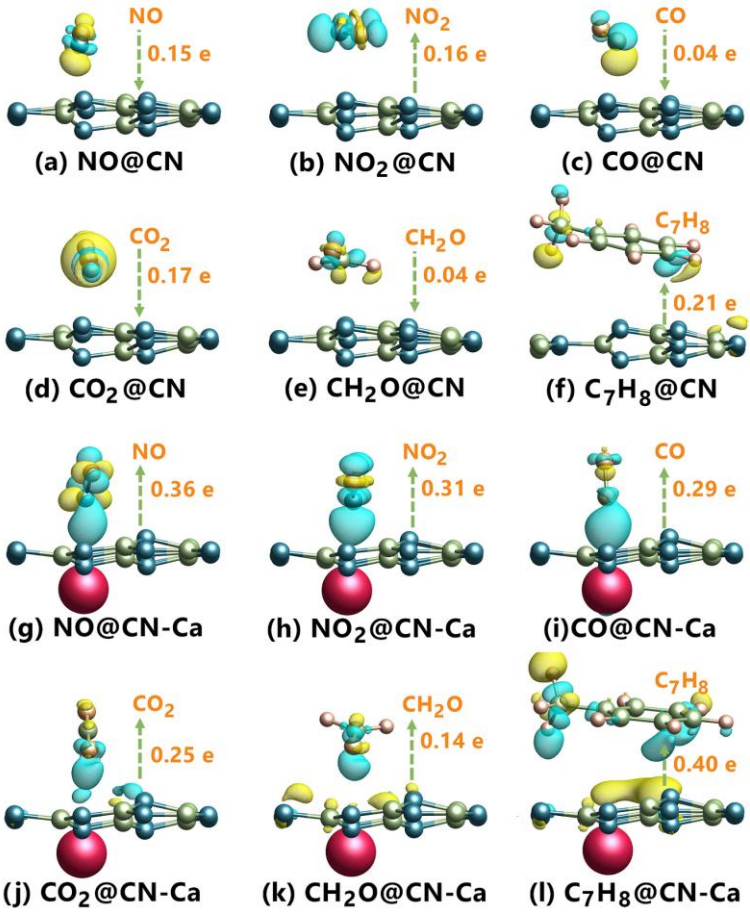
NO
0.15 e
(a) NO@CN
NO_2
0.16 e
(b) NO_2@CN
CO
0.04 e
(c) CO@CN
CO_2
0.17 e
(d) CO_2@CN
CH_2O
0.04 e
(e) CH_2O@CN
C_7H_8
0.21 e
(f) C_7H_8@CN
NO
0.36 e
(g) NO@CN-Ca
NO_2
0.31 e
(h) NO_2@CN-Ca
CO
0.29 e
(i)CO@CN-Ca
CO_2
0.25 e
(j) CO_2@CN-Ca
CH_2O
0.14 e
(k) CH_2O@CN-Ca
C_7H_8
0.40 e
(l) C_7H_8@CN-Ca

*Graphical Abstract

Graphical abstract

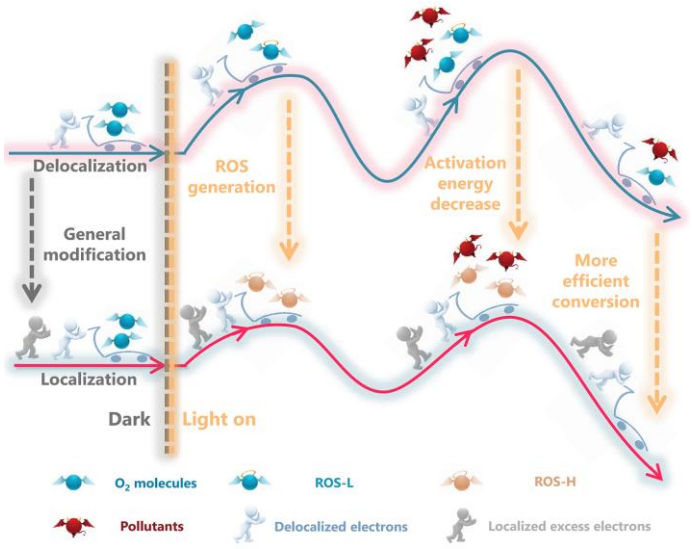

Research highlights

- The electrons localization patterns were established via Ca intercalation in g-C_3N_4.
- The localized excess electrons increased the yield of reactive oxygen species.
- The activity and selectivity in photocatalytic NO removal was greatly promoted.
- The experimental and theoretical approaches are closely combined.
- The rate-determining step in environmental photocatalysis was determined.